Journal of Materials Chemistry A

PAPER

View Article Online
View Journal | View Issue

Cite this: J. Mater. Chem. A, 2014, 2, 20770

Interfacial charge transfer and enhanced photocatalytic performance for the heterojunction WO_3/BiOCl: first-principles study†

Wenjuan Yang,[a] Yanwei Wen,[a] Dawen Zeng,[a] Qingbo Wang,[ac] Rong Chen,[b] Weichao Wang*[d] and Bin Shan*[a]

Received 21st August 2014
Accepted 21st October 2014

DOI: 10.1039/c4ta04327h

www.rsc.org/MaterialsA

First-principles calculations based on density functional theory were carried out to explore the interfacial properties of the WO_3/BiOCl heterojunction aiming at gaining insights into the roles the interface played in the overall photocatalytic performance. The interfacial effects of the WO_3 combination with BiOCl on electronic properties, charge transfer and visible-light response were investigated in detail. The density of states analysis showed that the interfacial structures resulted in a suitable band alignment to separate the excited carriers into two sides of the interface and thus, the electrons–holes recombination could be effectively suppressed. Moreover, excited holes could be readily transferred across the interface from the valence band maximum (VBM) of BiOCl to the VBM of WO_3 under visible-light irradiation without being trapped in interfacial mid-gap states.

1. Introduction

Photocatalysis has attracted increasing attention as a potential green energy technology by using solar light to decompose organic pollutants, to split water, to reduce CO_2 and so on. The critical obstacle that hinders wide application arises from the lack of low-cost and highly efficient semiconductor photocatalytic materials.[1,2] The bismuth oxychloride (BiOCl) photocatalyst has been extensively explored as an effective catalytic material due to its particular layer structure, electronic properties, photocatalytic activities and stability. BiOCl has a tetragonal layered structure consisting of $[Bi_2O_2]^{2+}$ layers sandwiched between two sheets of Cl ions with an internal electric field along the [001] direction.[3] The strong internal static electric fields perpendicular to the Cl layer and the bismuth oxide-based fluorite-like layer provides effective separation of the charge carriers.[4] BiOCl semiconductor, with an indirect-transition band gap, makes the electrons excited to the conduction band through a certain *k*-space distance, reducing the recombination probability of photo-excited charge carriers. Zhang *et al.*[5] reported that BiOCl exhibited better photocatalytic performance than Degussa P25 even after three cycles of decomposing methyl orange dye under ultraviolet-light illumination. However, its potential for photocatalytic application is seriously restricted due to its large band gap (3.40 eV), which absorbs less than ~4% of the whole solar photon spectrum.

Thus, narrowing the band gap of BiOCl to the visible-light range provides a straightforward way to achieve higher photocatalytic activity. Doping[6–9] or co-doping[10,11] with extrinsic impurity atoms has been proved to be an effective way to reduce the band gap. On the other hand, dopant-mediated rapid recombination of charge carriers in the lattice is a significant problem restricting its practical application.[12] As an alternative approach, combining BiOCl with other materials to construct heterojunctions has been another useful approach to enhance the carrier separation and realize overall response to the solar spectrum, and consequently achieve a higher efficiency for the decomposition of organic compounds in wastewater or polluted air. Previously, substantial BiOCl-based composite systems, such as BiOI/BiOCl,[13] Bi_2S_3/BiOCl,[14] Fe_3O_4/BiOCl,[15] $NaBiO_3$/BiOCl,[16] graphene/BiOCl,[17] Bi_2O_3/BiOCl,[18] $Bi_2O_2CO_3$/BiOCl,[19] $Bi_{24}O_{31}Cl_{10}$/BiOCl,[20] $W_{18}O_{49}$/BiOCl[21] *etc.* have been found to broaden the utilization of BiOCl into the visible-light region and display higher visible-light photocatalytic activities than pure BiOCl. Huang *et al.*[14] fabricated a Bi_2S_3/BiOCl heterojunction by a controlled anion exchange approach to show a high photocatalytic response to visible light. Fundamentally, the improvement might correlate to the interfacial charge transfer, which minimizes electron–hole recombination, thus significantly enhancing energy transfer efficiency. Therefore, it is

[a]State Key Laboratory of Materials Processing and Die and Mould Technology and School of Materials Science and Technology, Huazhong University of Science and Technology, Wuhan 430074, Hubei, China. E-mail: bshan@mail.hust.edu.cn

[b]State Key Laboratory of Digital Manufacturing Equipment and Technology and School of Mechanical Science and Engineering, Huazhong University of Science and Technology, Wuhan 430074, Hubei, China

[c]School of Mathematics and Physics, China University of Geosciences (Wuhan), Wuhan 430074, Hubei, People's Republic of China

[d]Department of Electronics, Nankai University, Tianjin, 300071, China. E-mail: weichaowang@nankai.edu.cn

† Electronic supplementary information (ESI) available. See DOI: 10.1039/c4ta04327h

important to find a suitable photosensitizer to make a contact with BiOCl. Tungsten oxide (WO_3) is such a feasible candidate for a visible-light photosensitizer ($\lambda < 440$ nm). WO_3, being an n-type semiconductor ($E_g = 2.60$–2.80 eV (ref. 22–24)), presents exceptional thermal, optical, stable physicochemical and electrical properties and resilience to photo-corrosion effects.[25,26] Under irradiation by visible light, photo-induced electrons and holes can be produced in the conduction band and valence band of WO_3, respectively. Pure WO_3 has been used in the photocatalytic degradation of organic pollutants,[27] and in the evolution of O_2 by photogenerated holes in the water-splitting reaction.[28] Nevertheless, its wider application is limited by the rapid electron–hole recombination, which is an important factor in determining the overall photocatalytic behavior. Recently, Zhang *et al.* synthesized a WO_3/BiOCl heterojunction by a novel low-temperature route, which shows distinct visible-light absorption and an unexpectedly high efficiency in decomposing Rhodamine B as compared to Degussa P25, pure-phase BiOCl and WO_3.[29] However, the WO_3/BiOCl heterojunction has rarely been investigated in terms of the atomic structure and electronic and optical properties to the best of our knowledge. Without fully understanding these fundamental electronic structures, it is harder to further optimize the structure and improve the photocatalytic performance.

In this paper, the WO_3/BiOCl heterojunction was studied based on first-principles calculations, aiming at gaining insights into the roles which the interface played in the overall photocatalytic performance. We found that the lattice of the BiOCl {010} crystal plane and WO_3 {010} crystal plane match well with each other and the interfacial bond with Bi–O–W was thermodynamically stable. The band offsets (BOs) (*i.e.*, valence band offsets (VBO) and conduction band offsets (CBO)) indicated that band alignments were favorable to transfer and separate charge carriers to the different domains of the catalysts. Since the interfacial atoms were saturated, there are no localized interfacial states within the band gap.

2. Computational method

Our calculations were based on the density functional theory (DFT) with the Perdew–Burke–Ernzerhof[30] version of the generalized gradient approximation (GGA-PBE) for the exchange–correlation potential, as implemented in a plane-wave basis code VASP.[31,32] The pseudo-potential was described by the projector-augmented-wave (PAW) method.[33] An energy cutoff of 400 eV and $5 \times 1 \times 5$ k-point with a Γ centered k mesh were used in our calculations. The force on each atom was converged to 0.02 eV Å^{-1} during the atomic structure optimization. For the supercell of our interface models, the atoms were relaxed and the interface distance re-optimized with a conjugate gradient (CG)[34] method.

We constructed a model interface between an orthorhombic BiOCl (CF12) and a monoclinic WO_3 ($P21/n$). The unit cell of BiOCl is derived from the fluorite structure,[35] which is a known tetragonal structure with lattice constants $a = b = 3.89$ Å and $c = 7.89$ Å. For WO_3, the lattice constants are $a = 7.30$ Å, $b = 7.54$ Å, $c = 7.69$ Å. Here, the BiOCl {010} and WO_3 {010} planes were selected owing to a small planar mismatch (X direction: 0.60%, Y direction: 0.90%) between these two planes. At the interface, they preferred to form Bi–O–W bonds due to the stronger dissociation energy (10.57 eV) compared with other possible interfacial bonding Cl–O–W (9.87 eV).[36] 10.00 Å vacuum regions were set to avoid interactions between top and bottom atoms in the periodic slab images. H atoms were utilized to saturate dangling bonds in the topmost tungsten. The passivation ensured that exposed top-surface states were removed and all the gap states originated from the interface. The whole slab was 49.06 Å thick with 146 atoms. The BiOCl slab consisted of eight layers of bismuth, eight layers of chlorine and eight layers of oxygen, while the WO_3 slab had twelve layers, which were thick enough to obtain bulk properties in the BiOCl and WO_3 parts.

The absorption spectrum of the WO_3/BiOCl heterojunction was also calculated by the Fermi golden rule within the dipole approximation from PBE wavefunctions. The imaginary part of the dielectric function due to direct interband transitions was obtained from the full many-electron wavefunction directly by the following equation:[37]

$$\varepsilon_2(\hbar\omega) = \frac{2e^2\pi}{\Omega\varepsilon_0}\sum_{\kappa,v,c}\left|\langle\psi_\kappa^c|ur|\psi_\kappa^v\rangle\right|^2\delta\left(E_\kappa^c - E_\kappa^v - E\right)$$

where Ω, ω, v, r, and c are the unit cell volume, photon frequency, and the vectors defining the polarization of the incident electric field, valence bands, and the conduction bands, respectively. The real part (ε_1) of the dielectric function can be evaluated from the imaginary part (ε_2) *via* the Kramers–Kronig transform. The real part and absorption coefficient (α) could be calculated by the following formula:

$$\varepsilon_1 = 1 + \frac{2}{\pi}p\int_0^\infty \frac{\omega'\varepsilon_2(\omega')}{\omega'^2 - \omega^2}\mathrm{d}\omega'$$

$$\alpha(\omega) = \sqrt{2}\omega\left[\sqrt{\varepsilon_1{}^2(\omega) + \varepsilon_2{}^2(\omega)} - \varepsilon_1(\omega)\right]^{\frac{1}{2}}$$

3. Results and discussion

3.1 Model of the intrinsic interface WO_3/BiOCl

Fig. 1(a) and (b) give the atomic models of the bulk BiOCl and WO_3 structures. The {010} crystal planes of BiOCl and WO_3 were selected owing to a small planar mismatch between these two planes along the X and Y directions, respectively. Experimentally, the {010} crystal plane of BiOCl has been reported to possess superior indirect dye photosensitization degradation activities under visible light.[38] BiOCl nanosheets with exposed {010} facets had a larger surface area and open-channel characteristics, which enhanced the adsorption capacity of methyl orange molecules and provided more contact sites between the photocatalysts and dye molecules. For the WO_3 structure, the {010} plane was the crystal growth direction based on the observations by Ye *et al.*[39] and Parkin *et al.*[40] Experimentally, it is also found that WO_3 {010} is the contact plane in the

heterojunction WO_3/BiOCl.[29] Thus, it would be informative to construct a theoretical heterojunction model through contacting the BiOCl {010} plane and the WO_3 {010} plane.

Fig. 1(c) depicts the side view of the interface between the BiOCl and WO_3 models. Fig. 1(d) shows the interface configuration with irrelevant atoms removed for clarity in visualization. To accommodate the lattice constant difference, the atomic cell in {010}-oriented BiOCl was doubled in the *X* direction and then rotated by 180° to match the {010} plane of WO_3. In order to obtain the lowest energy globally, several steps were used to set up the initial interface structure before relaxing the interface as shown in Fig. 1(e). WO_3 was shifted along the *X* direction ranging from −4.00 Å to 5.00 Å, and along the *Y* direction ranging from −2.00 Å to 2.00 Å to find the lowest energy point. Fig. 1(e) gives the total energy of the structure WO_3/BiOCl in the grid-shifting process. By analyzing the total energy, we found the optimized initial atomic position at the interface which should be close to the global minimum. Starting from the lowest energy point along the *X* and *Y* directions, the interface underwent full structural relaxation with the three bottom BiOCl atomic layers frozen (Fig. 1(f)).

At the WO_3/BiOCl interface (Fig. 1(f)), oxygen atoms are bonded with Bi atoms, with the Bi–O bond length 2.83 Å in contrast with 2.26 Å in the BiOCl bulk region, far away from the interface region. Each interfacial bismuth atom bonds to two oxygen atoms in the upper WO_3 region and three oxygen atoms in the BiOCl region. In order to further explore interfacial bonding information, the bond angles are calculated. Interfacial O–Bi–O indicates a higher angle, 120.75° compared to 113.58° in bulk BiOCl, which implies a planar strain at the interface. Resulting from the strong dissociation energy of the W–O–Bi bond and the small planar strain (~1%), the corresponding interfacial model (Fig. 1(f)) is a realistic reflection of interfacial bonding situations and adopted in all subsequent electronic structure calculations, unless otherwise noted.

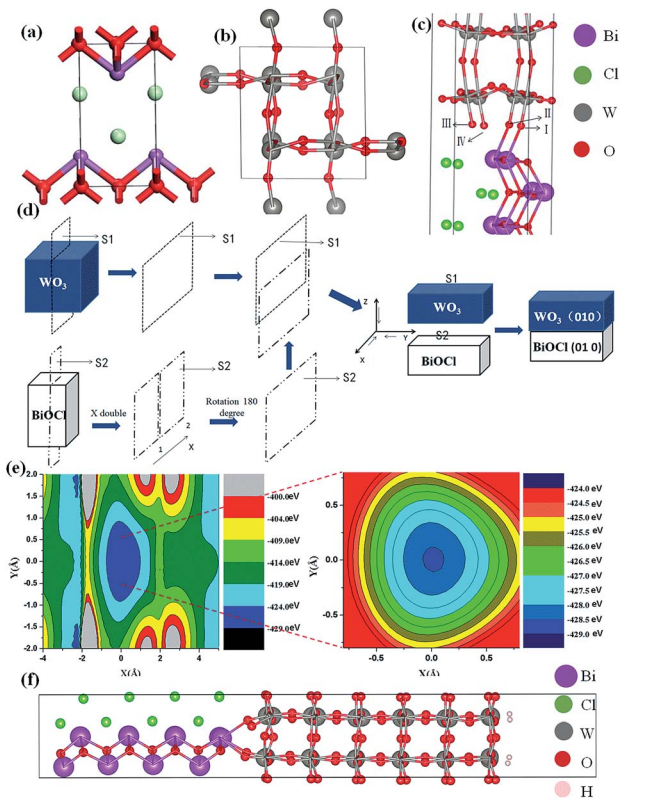

Fig. 1 (a) Side view of BiOCl, (b) side view of WO_3 and (c) side view of the WO_3/BiOCl interface. (d) Schematic construction of the interface between BiOCl and WO_3. (e) Energy contour of WO_3 shift along *X*-direction and *Y*-direction. (f) Finally relaxed configuration of WO_3/BiOCl. Green, pink, red and gray atoms are Cl, Bi, O, and W, respectively.

3.2 Electronic structure of the WO_3/BiOCl interface

BOs are one of the most important quantities to influence the photocatalytic performance of the heterojunction, as these band discontinuities are key parameters for tuning the carrier transport across the interface. It is thus essential to calculate the BOs by the local density of states (LDOS)[41,42] or the potential-line-up methods,[43–45] both of which yield essentially the same value of BOs. Here we use the former method to find BOs and the latter method is also utilized to double-check the accuracy of the BOs.

Fig. 2 shows the DFT-calculated total density of states (TDOS) and LDOS projected onto the different layers of the interface model. The labels marked "bulk BiOCl" and "bulk WO_3" mean the projections on the layers far from the interface, so the bonding environment is almost identical to that in the bulk. Four features are apparent: (i) there is a gap of about 1.00 eV for the whole slab shown in the TDOS, which means that the atoms at the WO_3/BiOCl interface are fully saturated and the surface atoms are well passivated. (ii) the band gap of bulk BiOCl is about 2.50 eV, spanning an energy range from 0.00 to 2.50 eV, and WO_3 has a band gap of 1.70 eV, spanning an energy range from −0.60 to 1.10 eV. Both band gaps are underestimated due to the DFT limitations in describing the excited states. (iii) the

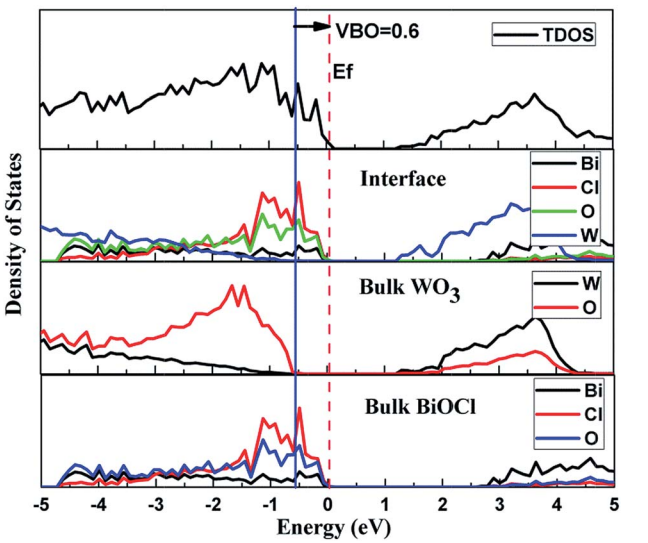

Fig. 2 DFT-calculated total and local density of states of WO_3/BiOCl interface.

valence band maximum (VBM) is mainly composed of BiOCl, while the states of WO_3 are 0.60 eV lower, indicating a 0.60 eV valence band difference between BiOCl and WO_3. To avoid the well-known problem that DFT could not accurately predict the excited states, we used experimental values of these band gaps to derive the conduction band offsets. Specifically, the CBO was evaluated by the simple relation CBO = $E_{gBiOCl} - E_{gWO_3}$ + VBO, where E_{gBiOCl}: 3.40 eV (ref. 46) and E_{gWO_3}: 2.60 eV (ref. 47) are the experimental optical band gaps of BiOCl and WO_3, respectively. Using this approach, the deduced CBO is 1.40 eV. (iv) the interface has a band gap of 1.00 eV without any local gap states; in other words, this interface will not trap the carriers and consequently avoids Fermi level pinning.

To explore charge redistribution across the WO_3/BiOCl interface, we calculated the three-dimensional charge density difference by subtracting the electronic charge of a WO_3/BiOCl composite from those of the WO_3 and BiOCl structures. The charge redistribution along the *Z*-direction normal to the interface is shown in Fig. 3. The yellow region represents charge accumulation, and the cyan region indicates charge depletion. The charge redistribution mostly takes place at the WO_3/BiOCl interface region and relaxes a bit into the bulk WO_3 and BiOCl samples, whereas there is almost no charge transfer on WO_3 or BiOCl farther away from the interface due to weak interaction between these two phases. In general, both the charge depletion and the charge accumulation constitute the interface charge redistribution behavior, causing the interface electric dipole formation. The planar-averaged charge density difference along the *Z* direction exhibits charge redistribution. The positive values represent electron accumulation, and negative values indicate electron depletion. The quantitative calculation of the change in the dipole moments at these interfaces shows that the holes mainly transfer from the WO_3 side to the BiOCl side across the interface.

As shown by the DOS in Fig. 2, the band gap of the whole WO_3/BiOCl slab system becomes smaller with bulk BiOCl as the VBM, and bulk WO_3 as the CBM. To show this directly, we plotted the charge density distribution of the electronic states comprising the band edges, *i.e.*, with energies in the range from 0.00 to 0.50 eV below the VBM (Fig. 4(a)) and 0.00 to 0.50 eV above the CBM (Fig. 4(b)). It is clear that these band edge states are delocalized in bulk BiOCl and bulk WO_3, with little distribution on the Bi–O–W bonding interface, consistent with the prediction from the DOS results.

3.3 Optical properties and photocatalytic mechanism

The optical absorption properties of semiconductor photocatalysts are related to their electronic structures. To examine the effect of the photocatalytic efficiency of the WO_3 combination with BiOCl, the calculated UV-vis absorption spectra of pure BiOCl, WO_3 and the WO_3/BiOCl heterojunction have been plotted in Fig. 5. For pure BiOCl, the large band gap restricts its application to the narrow light-response range of ultraviolet, while WO_3 could absorb visible light owing to its narrow band gap. The optical absorption edge of the WO_3/BiOCl heterojunction shifts to a longer wavelength region compared to that

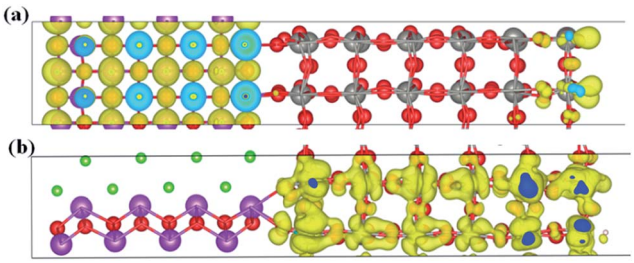

Fig. 4 (a) The summed charge density of the electronic states in the energy range 0.00–0.50 eV below VBM and 0.00–0.50 eV above CBM (b) of the slab system WO_3/BiOCl. The value of the charge density isosurface (in yellow) is 0.00087 electron per Å^3. Green, pink, red and gray atoms are Cl, Bi, O, and W, respectively.

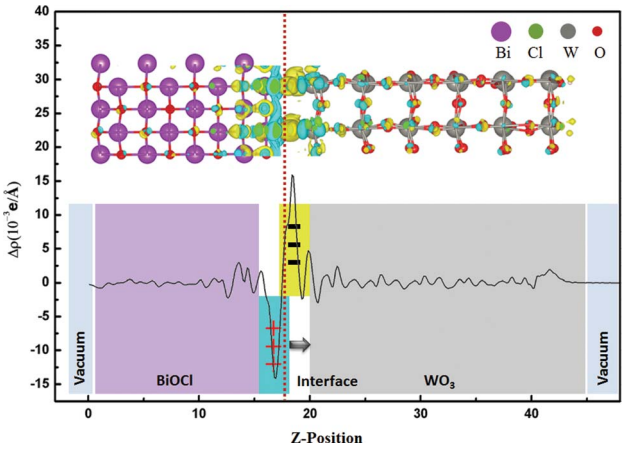

Fig. 3 Charge density differences ($\Delta\rho = \rho_{heterojunction} - \rho_{BiOCl} - \rho_{WO_3}$) and the corresponding planar average of the induced charge density difference for the WO_3/BiOCl. The yellow region represents charge accumulation, and the cyan region indicates charge depletion; the isosurface value is 0.00082 e per Å^3.

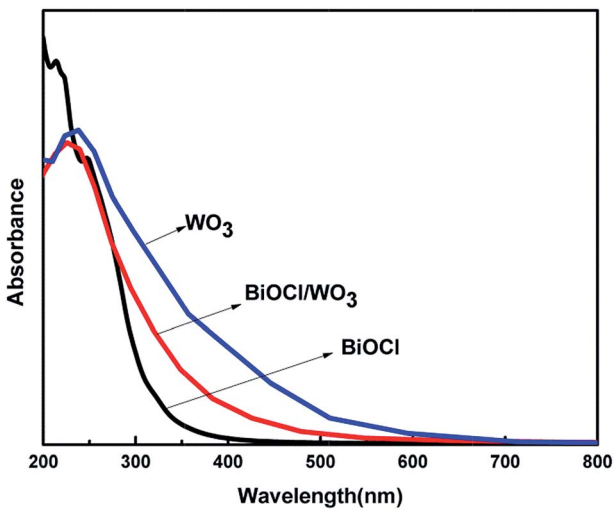

Fig. 5 Calculated optical absorption spectra of WO_3, BiOCl and WO_3/BiOCl heterojunction as a function of wavelength.

of the bulk BiOCl, which agrees well with the band gap reduction in the above section. We also considered and calculated the UV-vis absorption of the WO_3/BiOCl heterojunction with different oxygen amounts (with stoichiometry, stoichiometry-2, stoichiometry-4 oxygen atoms, respectively). It was found that the UV-vis absorption changes a little with interfacial structures as shown in Fig. S1.†

From the above electronic structure and optical property calculations of the WO_3/BiOCl interfaces, a schematic representation of the calculated VBO and CBO of the interface is shown in Fig. 6. Here, the VBO is also calculated by the potential-line-up method according to the formula:[48]

$$\mathrm{VBO} = \Delta E_v + \Delta V$$

where ΔE_v refers to the difference in the VBM obtained from two independent standard bulk band structure calculations at the same strained geometries as in the supercell calculation. ΔV results from the line-up of the macroscopic average of the self-consistent electrostatic potential across the interface. The deduced VBO by the potential-line-up method was calculated to be approximately 0.60 eV, in good agreement with the value from LDOS analysis. The corresponding CBO value was calculated to be 1.40 eV.

Under visual solar spectrum irradiation, electrons are excited to the conduction band on the WO_3 side of the heterojunction, producing holes in the valence band. The electrons of the excitation dye could rapidly transfer to the conduction band of the BiOCl in a thermodynamically favorable manner.[49,50] Then, the electrons in the conduction band of BiOCl will transfer to the conduction band of WO_3 since the latter conduction band position is lower. The holes in the VBM of the WO_3 side transfer to the VBM on the BiOCl side owing to the favorable BOs and absence of gap states trapping the holes at the interface. The hole-transport mechanism has also been proposed in explaining visible-light photocatalysis of heterojunction structures in many literature studies.[51–53] The photogenerated electrons in WO_3 cannot provide a sufficient potential to reduce O_2 by single-electron reduction ($O_2 + e^- = O_2^-$, -0.284 V_{NHE}; $O_2 + H^+ + e^- = HO_2$, -0.046 V_{NHE}).[54,55] Furthermore, two-electron reductions could hardly occur on WO_3.[56] A large number of holes on the surface of BiOCl can participate in photocatalytic reactions to directly or indirectly mineralize organic pollutants.[57] Holes and electrons are generated on the BiOCl and WO_3 sides, respectively. The transfer of photo-induced electron–hole pairs was accompanied by the consecutive reduction of W^{6+} to W^{5+} with the capture of photo-induced electrons at the trapping sites in WO_3.[58] Simultaneously, the W^{5+} ions contained by the WO_3 surface were reoxidized into W^{6+} by the oxygen. This movement results in the efficient separation of photogenerated electron–hole pairs and a slowed down recombination rate which consequently increases the photonic efficiency for the degradation of organic pollutants. Moreover, we tested the transient photocurrent density and found that the WO_3/BiOCl heterojunction exhibited a higher transient photocurrent density (about 5 μA cm^{-2}) than that of the WO_3 sample by a factor of 2.5 (seen in Fig. S2†). The larger photocurrent density indicates more transferred electrons from the WO_3/BiOCl photoanode, further providing strong evidence for an enhanced lifetime of electrons. The present result well accords with the experimental observations[29] and also illustrates the mechanisms of photocatalytic activity enhancement in WO_3/BiOCl composite photocatalysts compared to individual components.

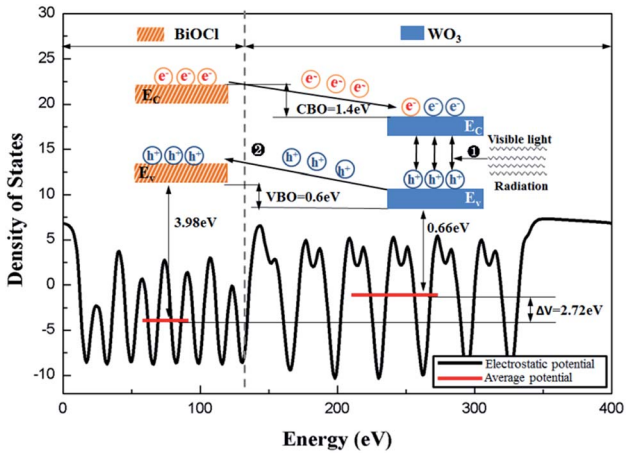

Fig. 6 Schematic representation of band offsets for the WO_3/BiOCl interface from the potential-line-up method. $Z = 0.00$ denotes the interface location.

4. Conclusion

This work demonstrates that the interface played an important role in the overall photocatalytic process based on the investigations of the WO_3/BiOCl interface by first-principles calculations. We found that the calculated BOs of WO_3/BiOCl interfaces were preferable for the separation of photogenerated carriers and effectively avoided electron–hole recombination. Furthermore, charges could be readily transferred across the interface from the VBM of BiOCl to the VBM of WO_3 under visible-light irradiation owing to the absence of interfacial gap states. As a result, photogenerated charge carriers were effectively separated with the holes on the BiOCl side and the electrons on the WO_3 side. The calculation results provide insights into the design of visible-light response for BiOCl-based semiconductor photocatalysts.

Acknowledgements

This work is supported by the National Basic Research Program of China (2013CB934800 and 2011CB606401), the National Natural Science Foundation of China (51302094 and 51101064), the Hubei Province Funds for Distinguished Young Scientists (2014CFA018), and the Tianjin Natural Science Foundation (13JCYBJC41100). We thank the Texas Advanced Computing Center (TACC) at the University of Texas at Austin (http://www.tacc.utexas.edu) for providing grid resources that have contributed to the research results reported within this paper.

Notes and references

1 M. G. Walter, E. L. Warren, J. R. McKone, S. W. Boettcher, Q. Mi, E. A. Santori and N. S. Lewis, *Chem. Rev.*, 2010, **110**, 6446.
2 X. B. Chen, S. H. Shen, L. J. Guo and S. Mao, *Chem. Rev.*, 2010, **110**, 6503.
3 K. L. Zhang, C. M. Liu, F. Q. Huang, C. Zheng and W. D. Wang, *Appl. Catal., B*, 2006, **68**, 125.
4 J. Jiang, K. Zhao, X. Xiao and L. Zhang, *J. Am. Chem. Soc.*, 2012, **134**, 4473.
5 K. L. Zhang, C. M. Liu, F. Q. Huang, C. Zheng and W. D. Wang, *Appl. Catal., B*, 2006, **68**, 125.
6 M. Guerrero, S. Pané, B. J. Nelson, M. D. Baró, M. Roldán, J. Sort and E. Pellicer, *Nanoscale*, 2013, **5**, 12542.
7 J. Di, J. X. Xia, S. Yin, H. Xu, X. Li, Y. G. Xu, M. Q. He and H. M. Li, *RSC Adv.*, 2014, **4**, 14281.
8 Y. Yu, C. Y. Cao, H. Liu, P. Li, F. F. Wei, Y. Jiang and W. G. Song, *J. Mater. Chem. A*, 2014, **2**, 1677.
9 W. Xiong, Q. D. Zhao, X. Y. Li and D. K. Zhang, *Catal. Commun.*, 2011, **16**, 229.
10 C. D. Wang, H. Qiu, T. Inoue and Q. W. Yao, *Comput. Mater. Sci.*, 2014, **85**, 138.
11 M. Nussbaum, N. Shaham-Waldmann and Y. Paz, *J. Photochem. Photobiol., A*, 2014, **290**, 11.
12 Z. Zhang and J. T. Yates, *J. Phys. Chem. C*, 2010, **114**, 3098.
13 X. Xiao, R. Hao, M. Liang, X. X. Zuo, J. M. Nan, L. S. Li and W. D. Zhang, *J. Hazard. Mater.*, 2012, **233**, 122.
14 H. F. Cheng, B. B. Huang, X. Y. Qin, X. Y. Zhang and Y. Dai, *Chem. Commun.*, 2012, **48**, 97.
15 L. Zhang, W. Z. Wang, L. Zhou, *et al.*, *Appl. Catal., B*, 2009, **90**, 458.
16 X. F. Chang, G. Yu, J. Huang, Z. Li, S. F. Zhu, P. F. Yu, C. Cheng, S. B. Deng and G. B. Ji, *Catal. Today*, 2010, **153**, 193.
17 F. D. Gao, D. W. Zeng, Q. W. Huang, S. Q. Tian and C. S. Xie, *Phys. Chem. Chem. Phys.*, 2012, **14**, 10572.
18 S. Y. Chai, Y. J. Kim, M. H. Jung, A. K. Chakraborty, D. Jung and W. I. Lee, *J. Catal.*, 2009, **262**, 144.
19 X. C. Zhang, T. Y. Guo, X. W. Wang, Y. W. Wang, C. M. Fan and H. Zhang, *Appl. Catal., B*, 2014, **150**, 486.
20 F. T. Li, Q. Wang, X. J. Wang, B. Li, Y. J. Hao, R. H. Liu and D. S. Zhao, *Appl. Catal., B*, 2014, **150**, 574.
21 Z. F. Huang, J. J. Song, L. Pan, X. Jia, Z. Li, J. J. Zou, X. W. Zhang and L. Wang, *Nanoscale*, 2014, **6**, 8865.
22 A. Kudo and Y. Miseki, *Chem. Soc. Rev.*, 2009, **38**, 253.
23 C. Santato, M. Ulmann and J. Augustynski, *Adv. Mater.*, 2001, **13**, 511.
24 C. Santato, M. Odziemkowski, M. Ulmann and J. Augustynski, *J. Am. Chem. Soc.*, 2001, **123**, 10639.
25 J. Z. Su, L. J. Guo, N. Z. Bao and C. A. Grimes, *Nano Lett.*, 2011, **11**, 1928.
26 E. Rossinyol, A. Prim, E. Pellicer, J. Arbiol, F. Hernandez-Ramirez, F. Peiro, A. Cornet, J. R. Morante, L. A. Solovyov, B. Z. Tian, T. Bo and D. Y. Zhao, *Adv. Funct. Mater.*, 2007, **17**, 1801.
27 D. Chen and J. Ye, *Adv. Funct. Mater.*, 2008, **18**, 1922.
28 D. Chen, L. Gao, A. Yasumori, K. Kuroda and Y. Sugahara, *Small*, 2008, **4**, 1813.
29 S. Shamaila, A. K. L. Sajjad, F. Chen and J. L. Zhang, *J. Colloid Interface Sci.*, 2011, **356**, 465.
30 J. P. Perdew, K. Burke and M. Ernzerhof, *Phys. Rev. Lett.*, 1996, **77**, 3865.
31 G. Kresse and J. Furthmüller, *Comput. Mater. Sci.*, 1996, **6**, 15.
32 G. Kresse and J. Furthmüller, *Phys. Rev. B: Condens. Matter Mater. Phys.*, 1996, **54**, 11169.
33 P. E. Blöchl, *Phys. Rev. B: Condens. Matter Mater. Phys.*, 1994, **50**, 17953.
34 W. Press, B. Flannery, S. Teukolsky and W. Vetterling, *Numerical Recipes*, Cambridge University Press, New York, 1986.
35 K. L. Zhang, C. M. Liu, F. Q. Huang, C. Zheng and W. D. Wang, *Appl. Catal., B*, 2006, **68**, 125.
36 D. R. Lide, *CRC Handbook of Chemistry and Physics*, 90th edn, 2009.
37 A. J. Read and R. J. Needs, *Phys. Rev. B: Condens. Matter Mater. Phys.*, 1991, **44**, 13071.
38 J. Jiang, K. Zhao, X. Y. Xiao and L. Z. Zhang, *J. Am. Chem. Soc.*, 2012, **134**, 4473.
39 G. C. Xi, J. H. Ye, Q. Ma, N. Su, H. Bai and C. Wang, *J. Am. Chem. Soc.*, 2012, **134**, 6508.
40 S. Ashraf, C. S. Blackman, R. G. Palgrave and I. P. Parkin, *J. Mater. Chem.*, 2007, **17**, 1063.
41 J. M. Bass, M. Oloumi and C. C. Matthai, *J. Phys.: Condens. Matter*, 1989, **1**, 10625.
42 J. Robertson and P. W. Peacock, *Phys. Status Solidi B*, 2004, **241**, 2236.
43 A. Baldereschi, S. Baroni and R. Resta, *Phys. Rev. Lett.*, 1988, **61**, 734.
44 L. Colombo, R. Resta and S. Baroni, *Phys. Rev. B: Condens. Matter Mater. Phys.*, 1991, **44**, 5572.
45 J. Junquera, R. Cohen and K. M. Rabe, *J. Phys.: Condens. Matter*, 2007, **19**, 213203.
46 K. L. Zhang, C. M. Liu, F. Q. Huang, C. Zheng and W. D. Wang, *Appl. Catal., B*, 2006, **68**, 125.
47 L. G. Teoh, J. Shieh, W. H. Lai, I. M. Hung and M. H. Hon, *J. Alloys Compd.*, 2005, **396**, 251.
48 M. Peressi, N. Binggeli and A. Baldereschi, *J. Phys. D: Appl. Phys.*, 1998, **31**, 1273.
49 D. H. Wang, G. Q. Gao, Y. W. Zhang, L. S. Zhou, A. W. Xu and W. Chen, *Nanoscale*, 2012, **4**, 7780.
50 J. Jiang, K. Zhao, X. Y. Xiao and L. Z. Zhang, *J. Am. Chem. Soc.*, 2012, **134**, 4473.
51 X. J. Guan and L. J. Guo, *ACS Catal.*, 2014, **4**, 3020.
52 J. G. Yu, Y. Wang and W. Xiao, *J. Mater. Chem. A*, 2013, **1**, 10727.
53 S. Shenawi-Khalil, V. Uvarov, S. Fronton, I. Popov and Y. Sasson, *J. Phys. Chem. C*, 2012, **116**, 11004.
54 S. Nishimoto, T. Mano, Y. Kameshima and M. Miyake, *Chem. Phys. Lett.*, 2010, **500**, 86.
55 T. Torimoto, N. Nakamura, S. Ikeda and B. Ohtani, *Phys. Chem. Chem. Phys.*, 2002, **4**, 5910.
56 J. Y. Sheng, X. J. Li and Y. M. Xu, *ACS Catal.*, 2014, **4**, 732.
57 T. B. Li, G. Chen, C. Zhou, Z. Y. Shen, R. C. Jin and J. X. Sun, *Dalton Trans.*, 2011, **40**, 6751.
58 V. Keller, P. Bernhardt and F. Garin, *J. Catal.*, 2003, **215**, 129.